EELS techniques towards characterizing and mapping iron valence states in iron oxide samples

Joan Sospedra Ramírez
Advisors: Sònia Estradé Albiol, Javier Blanco Portals
Laboratory of Electron Nanoscopies (LENS)- MIND/IN2UB, Dept. d'Electrònica, Universitat de Barcelona

***Abstract*—In this work a sample of iron oxide nanoparticles is studied with a variety of techniques. In order to map its oxidation states, a characterization through indexing its crystallographic structure is attempted, but it is an EELS big data treatment through model creation of individual components in conjunction with clustering what will ultimately reveal a distribution map of different oxidation states across the sample.**

***Index Terms*— EELS, transition metals, iron oxide, ELNES, oxidation states mapping, model creation, clustering.**

I. Introduction

A. An overview on Electron Energy Loss Spectroscopy

Electron energy loss spectroscopy (or EELS for short) in the transmission electron microscope (TEM), is an analytical tool that allows matter characterization at subnanometric scale. EELS has been in use for the last half century, and nowadays is a well-stablished technique able to probe the electronic structure of solids. The first high-energy (2-8 keV) EELS measurements in transmission were performed in 1941 by Ruthemann [1]. In these measurements, discrete excitations in simple metals were recorded which were later explained by Pines and Bohm [2] in terms of collective excitation of conduction electrons, i.e. plasmons [3].

EELS studies electron beams, the energy of which is well known, once they have interacted with a sample of a given material. Currently, these fast electrons energies are of the order of tens to hundreds of keV. In this technique, the studied samples must be thin enough for the incident beam passing through them without absorption or reflection, a thickness preferably under 100 nm. As the incident electron interacts inelastically with the sample, it changes both its energy and momentum. The scattered incident electron is directed to the spectrometer for a further classification in terms of their kinetic energy, in order to obtain an energy spectrum where the intensity (scattered electrons) is displayed as a function of the kinetic energy loss [4].

A typical EELS spectrum has a series of distinct features. The first feature one finds is the zero-loss peak or elastic peak, representing the electrons that are transmitted with without suffering measurable energy loss, including elastically scattered electrons. Those electrons may suffer a phase shift, but that is only detectable through holography or high-resolution imaging. The plasmonic region follows the zero-loss peak, and it appears as the result of conduction electrons plasma resonance. In the solid state free electron model, plasmon excitations can be understood as harmonic oscillations of the conduction band electrons, weakly bound to a fixed ion background. This way, we can relate oscillation frequency and, consequently, its energy, to the gas electron density and effective mass of the carriers. As a result, plasmon peak position is a great indicator of the changes the sample suffers, expressed as carrier number variations. Past this region, at losses of more than a hundred eV, the number of electron counts decays significantly. This is where the edges of the nuclei can be found. The onset of those edges describes the elements present in the sample, while the area below the edge is proportional to the number of atoms that have interacted of this specific element.

EELS goal is to map the spatial distribution of properties shown in individual EEL spectra, and to do so, the technician must usually work with huge amounts of data. The characterization of a sample may involve the acquisition of energy loss spectra for every pixel of the sample (spectrum images), each of those spectra comprised by thousands of

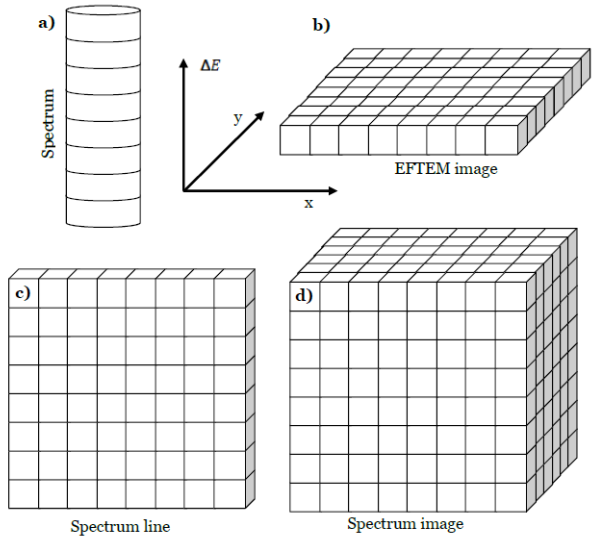

Figure 1. Representation of spectrum images of different dimensionalities (a) individual spectrum, b) energy filtered transmission electron microscope (EFTEM) image, c) spectrum line, d) spatial two-dimensional spectrum image), and its axis reference. Figure obtained from [6.2].

channels. Figure 1 shows a representation of a single spectrum, a spectrum line, and a datacube or spectrum image, but datacubes of 4 dimensions (3 spatial and the last for energy) could be also used [6.1]. This is the reason why big data treatment is highly encouraged to tackle EELS data treatment and management.

B. EELS physics

Even though elastic interactions occur, the main interactions between the incident electrons and the sample are inelastic interactions. The former are useful to image the sample, but EELS relies in changes of momenta and energies to characterize atomic species, making those inelastic interactions the ones used in spectroscopy. Focusing on core loss physics, inelastic phenomena occurs between incident electrons and the electronic clouds of atoms in the sample, driven by Coulombian electrostatic repulsion between the negative charges, by both internal or external layers. Incident electrons lend characteristic amounts of energy to the atomic electron primary excitations. But before considering inelastic scattering mechanisms in detail, it is interesting to point at the concept of the total cross section for this scattering by the atomic electrons. There are several atomic models developed to describe the behavior of the beam after interacting with matter that had their origin in elastic interaction theory. Lenz modified Morse's elastic theory in 1954 [7] and obtained a first approximation for the differential cross section, which then was adapted by Reiner and Kohl (2008) into the following expression

$$\frac{d\sigma_i}{d\Omega} = \frac{4\gamma^2 Z}{a_0^2 q^4}\left(1 - \frac{1}{[1+(qr_0)^2]^2}\right) \qquad (1)$$

where γ corresponds to the relativistic Lorentz factor, a_0 is Bohr's radius, r_0 is the screening radius, equivalent to $a_0 Z^{-1/3}$ according to the Thomas-Fermi model, and q is given by

$$q^2 \approx k_0^2(\theta^2 + \bar{\theta}_E^2) \qquad (2)$$

where $k_0 = \frac{2\pi}{\lambda} = \frac{\gamma m_0 v}{\hbar}$ is the incident electrons wavevector magnitude, θ is the dispersion angle and $\overline{\theta_E} = \frac{\bar{E}}{\gamma m_0 v^2}$ is the characteristic angle associated to an average energy loss $\bar{E}$. [4.3] Thus, equations (1) and (2) can be combined into

$$\frac{d\sigma_i}{d\Omega} = \frac{4\gamma^2 Z}{a_0^2 k_0^4}\frac{1}{(\theta^2+\bar{\theta}_E^2)^2}\left(1 - \left[\frac{\theta_0^4}{\theta^2+\bar{\theta}_E^2+\theta_0^2}\right]\right) \qquad (3)$$

with $\theta_0 = \frac{1}{k_0 r_0}$. [4.4]

To describe in more detail the inelastic scattering of electrons by an atom, Inokuti based his calculations within the framework of the Bethe theory and the first Born approximation, [8] where the behavior of each atomic electron is specified in terms of transition from an initial state of wavefunction ψ_0 to a final state ψ_n. The Bethe theory provided a convenient and consistent quantum-mechanical basis for electronic excitation in atoms, opening a plethora of new approaches to the problem, developed the following years. New cross section models had been developed (e.g. Newbury 1986, Goldstein 1986), based on probabilistic approaches to obtain a relationship between the signal intensity collected in terms of the number of atoms of a given element. Hartree-Fock (HF) is one of the methods based on this approach and in fact, is one of the methods used nowadays still [4.5]. HF, and alternatively the Hartree-Slater method, are able to obtain more accurate cross sections, by calculating the atomic potential from an iterative solution of the Schrödinger equation, and can be further expanded by including electron spin and relativistic effects within the atom by using the Dirac equation [9], leaving to the so-called Mott sections.

C. Energy Loss Near Edge Structure

When the incident primary electrons of the incident focused beam interact with the atoms in a sample, core and valence electrons whose energy levels increase can scatter with the potential of the crystal or exit the sample depending on their energy. In a first approximation, the minimum energy required by the primary electron to eject the core electrons can be compared to the ionization potential of the excited atom in the specimen. However, the ejected core electron can also probe the first unoccupied bound states of the crystal. Due to this, the allowed energy levels and final state will strongly depend on the overall electronic structure, i.e. structural and chemical environment of the atom excited by the incident electrons. The primary electrons can also provide an amount of energy superior to the energy needed to excite the atom's electrons, which constitutes the continuum. The final state of the ejected electron is ultimately reflected on the probability of energy loss by the primary electron and is thus visible on the EEL spectrum, but particularly of the near-edge structure (ELNES) [10].

XPS (X-ray photoelectron spectroscopy) or XAS (X-ray absorption spectroscopy) are often mentioned when discussing the reason why to use ELNES. The former is usually used to obtain information on the chemical properties of thin films, whereas the latter is used in synchrotron facilities to extract valence and coordination information [11]. The key to answering this question is spatial resolution. ELNES is able to obtain the same information as the aforementioned techniques with a comparable energy resolution as XAS but obtaining interatomic spatial resolution with the aid of aberration-corrected microscopes.

So, what is the nature of ELNES? The near edge-structure provides further understanding of the structure of the material at solid state level. Core-loss spectra recorded from solid specimens often show a pronounced fine structure, taking the form of peaks or oscillations in intensity within 50 eV of the ionization threshold. Most of this structure reflects the influence of atoms surrounding the excited atom and requires a solid-state explanation [4.6].

The modelling of ELNES in intimately associated with the calculation of a fundamental quantity known as the inelastic double differential scattering cross section (DDSCS), which measures the probability per unit time, energy, solid angle and incident electron density for a fast incident electron beam to be scattered inelastically when propagating through the sample. Among all the processes that could contribute with an energy loss of the electron, ELNES is related to processes involving only one electron-hole pair in the solid [10].

One of the most accepted approaches is the densities of states (DOS) interpretation, which is greatly simplified by making a one electron approximation, i.e. an excitation of an inner-shell electron is assumed to have no effect on the other atomic electrons. This interpretation is based on the fact that modulations of the single-scattering intensity can be related to the band structure of the solid in which scattering events occur. [4.6] So, taking as a framework the Bethe theory and applying the first Born approximation, one arrives to the following expression for the DDSCS [12, 13]:

$$\frac{\partial \sigma^2}{dEd\Omega} = \frac{4\gamma^2 k'}{a_0^2 q^4 k} S(q,E) \qquad (4)$$

where $S(q,E)$ is the so-called dynamic form factor (DFF):

$$S(q,E) = \sum_{c,v} \left|\langle \varphi_v | e^{iqr} | \varphi_c \rangle\right|^2 \delta(\varepsilon_v - \varepsilon_c - E) \qquad (5)$$

being $|\varphi_c\rangle$ the initial core state of energy ε_c, and $|\varphi_v\rangle$ is the final conduction state of energy ε_v for the solid electron. The particular form of the matrix element appearing in this expression has important consequences on the physical interpretation of the near-edge fine structure. The evaluation of this matrix element is obtained by integrating the spatial coordinates over a very sharp region centered on the nucleus.

Equation (5) presents some similarities with the density of states expression used in solid-state,

$$\rho(E) = \sum_v \delta(\varepsilon_v - E) \qquad (6)$$

where the sum is taken over the electronic states of the solid with energies above the Fermi level. This reasoning points to the DFF being interpreted as a weighted local density of states (LDOS).

It is because of different densities of unoccupied states from atom to atom that the ELNES allows us to distinguish their coordination. Hence, in terms of solid state, we can then correlate the fine structure of the edge, and, in particular, the chemical shift (small variations in edge onset) with such variables as oxidation states, atomic charge and coordination with the data from reference materials in order to characterize our sample.

D. White lines

$L_{2,3}$ edges in transition metals (TM) and $M_{5,4}$ edges in rare earths show sharp peaks arising from transitions to well defined energy states instead of broad continuums, which are the so-called white lines, and they are usually separated by a few eV. The nature of the white lines is purely based on quantum mechanics. For instance, the spin-orbit splitting divides in three states the L shell in transition metals. Due to Pauli exclusion principle, the sum j of the spin s and angular momentum l, is restricted. Being the L_3 and L_2 electrons in the p orbital, j can only be 1/2, 3/2 and 5/2. The latter can only have two electrons with j = ±1/2, whereas the L_3 electrons can have j = ±1/2, ±3/2. This fact may lead to thinking that in the spectrum there should be the double of counts in the L_3 white line comparing to the L_2 line. However, in the literature there seems to be consistent fluctuations from the ideal value of 2 [6.4]. These deviations in the L_3/L_2 ratio arise from the DOS above E_F. Due to the dipole selection rule, the change in l angular momentum quantum number can only be ±1. As the state of the p electrons in the L shell has l=1, the final states are either s or d, with l = 0 or l = 2 respectively. As the ejected core electrons end primarily in the unoccupied d states, they are more available than the s, so the density of d states above the Fermi energy will determine the ratio. Transitions from the 2s state, i.e. the L_1 level, are also possible, but give a weak ionization edge, due to the dipole selection rule forbidding s to d transitions [14]. It has been found that similarly to the $L_{3,2}$ white lines for transition metals, for rare-earths appear white lines in the $M_{3,2}$ and $M_{5,4}$ transitions, and their intensity ratio is related to the oxidation state of the transition or element [15].

E. Iron oxidation states

Nowadays, it is well stablished that transition metals oxidation states are linked to the shape of the $L_{3,2}$ excitation edges [16-21]. Several procedures exist to calculate oxidation states, but the most popular is the $L_{3,2}$ ratio. Although this method was successful in determining the oxidation states of Mn and Fe in some minerals in a limited oxidation state range [20-22], there are some restrictions in linking the detailed shape of EELS excitation edges to the oxidation state. Especially for Fe, unambiguous oxidation state determination can be difficult, because of shapes in the spectra not always having a one to one relationship with a particular valence state, as the method is dependent on sample thickness and on the exact procedure which is used to measure the white line intensities. Besides, the excitation edge energy position is also correlated to its

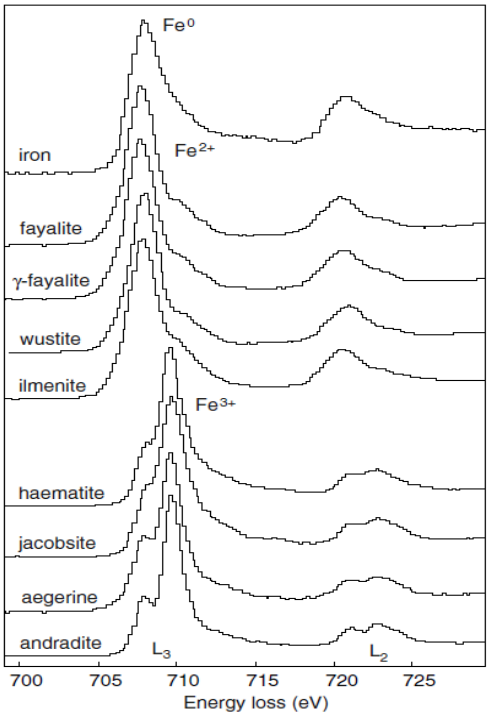

Figure 2. Fe $L_{3,2}$ edges of elemental Fe and selected minerals containing single-valent Fe. The spectra from a range of minerals, with Fe bonded to O, show a consistency of edge shapes for given oxidation states. Figure obtained from [22].

oxidation state, i.e. the chemical shift: In general, the excitation edges shift to a higher energy-loss for a higher oxidation state. For further reading, see [23]. However, several publications [24-26] have reported characteristic shapes in the L white lines for iron in terms of the oxidation state, as can be seen, for instance, in Figure 2.

All those once considered ambiguities, are what now can help us determine and quantify (therefore map) iron in a sample in terms of its valence states, using not only the intensity ratios and integration over the background of the white lines of the L shell, but also through the general shape of the edge comparing with the literature and taking into account chemical shifts from tabulated values.

F. State of the art. Motivations and chosen approach

Digital Micrograph (DM) is an application used for acquiring, visualizing, analyzing, and processing digital image data, primarily within the context of electron microscopy. It can be thought of as an environment that can be enhanced with different attachments (plug-ins) to perform a variety of analytical tasks [26]. Digital Micrograph has proven to be one of the best ways to analyze data in EELS data treatment, but also one of the few ways to do so. This exclusivity meant that the efficiency of the data analyst was confined into the scope of DM, or in other words, that if there was no direct way to perform a measurement, one had two options: to build a plug-in for DM or to start from the ground up.

In the case of oxidation states measurements in transition metals, Yedra et al. presented Oxide Wizard (OW) [27], a script for Digital Micrograph (DM) that measures and maps several characteristics of the TM edge, which can be related to the oxidation state. The script can be downloaded for free from the University of Barcelona digital database (diposit.ub.edu). This script was developed to characterize the white lines found in the ELNES of transition metals, dealing with large spectral images in a systematic way. OW gives as an output several relevant data, such as white lines ratios, the oxygen K onset, the transition metal onset, the difference between both, the full width half maximum of the transition metal's first white line, and the separation between the white lines. Those parameters allow the analyst to distinguish regions with different oxidation states, in order to map the sample accordingly. However, this script is not flawless: OW presents an insufficient manner to fit the continuum contribution into the model, as it uses at the present time a linear fitting that does not adjust it reliably. Also, even though OW has shown to be consistent with small datasets, it struggles at mapping spectrum images with a high number of pixels, giving incorrect fittings of the experimental data.

The other approach towards a proper characterization of transition metals involves coding. Hyperspy [28] is an open-source compilation library for Python, which is based on the libraries NumPy, SciPy, matplotlib and scikit-learn. Hyperspy provides tools to facilitate the interactive data analysis of multi-dimensional datasets that can be described as multi-dimensional arrays of a given signal.

HyperSpy aims at making it easy to apply analytical procedures that operate on an individual signal to multi-dimensional arrays, as well as providing easy access to analytical tools that exploit the multi-dimensionality of the dataset. Furthermore, its modular structure makes it easy to add features to analyze different kinds of signals. Taking profit from this, using Hyperspy as a framework in which the data analyst is provided with the needed tools to manage huge EELS datasets, a series of methods specifically designed towards white line inspection can be conveniently integrated to the ones conforming this library. This is the approach taken in this paper to work with the sample presented in section II.

G. Work scope

The present paper aims to study and map the composition of a sample of iron oxide nanoparticles in terms of the valence state of the iron. The study of oxidation states of iron oxide nanoparticles is becoming a matter of rising interest for the understanding of the Alzheimer disease. Iron ions are present in healthy brains in the form of hydrous ferric oxide, known as ferrihydrite, with a valence state of Fe^{3+}, and are stored in the core of ferritin molecules [29]. Iron presence is needed for good neural function since it is believed to play an important role in processes like neural differentiation, myelinisation and neural plasticity, and a lack of it has been observed to lead to cognitive impairment and neural dysfunction [30]. However, the presence of higher concentrations of iron ions arises as a toxicity and pathogenic concern. The reason for this is related to iron atoms' valence and their oxidative-reductive (redox) potential. Ferrihydrite iron ions are found to be in a redox-inactive state while Fe^{2+} ions, like the ones found in magnetite (Fe_3O_4), a combination of Fe^{2+} and Fe^{3+} ions, have been described to have a redox-active state. The presence of such redox-active specimens results in the generation of toxic free radicals like reactive oxygen species, by means of ferrous iron reaction with hydrogen peroxide via the Fenton reaction, which cause brain oxidative stress. This might lead to brain injury and neural death contributing, in this way, to the progression of neurodegenerative diseases like the Alzheimer's disease [31,32].

The main method chosen to study the oxidation states of our sample is through Hyperspy, a library for Python that packs several tools for the user to manage the EELS data obtained in the TEM. The objective is to process the data since the moment it is received from the TEM session, take a suitable region of interest, and then apply noise and background removal in order to prepare it for the application of data treatment methods. Those methods model and study the information about oxidation states that the white lines can offer. Through this library, the desired outcome is getting a model fit for the experimental data, through which obtain relevant information towards the oxidation state mapping, such as the $Fe^{3+}/\Sigma Fe$ white line ratio, relevant onset positions, edges' full width half maxima, etc.

G.a) Principal component analysis

Principal Component Analysis, or PCA, must arguably be the most popular multivariable analytic method. It consists on finding a new parametric model for the dataset, where every spectrum can be described as a weighted sum of a finite number of components and noise [33]. PCA looks for the minimum number of variables that describe the original data in order to reduce the problem's dimensionality without the loss of physical information. The model assumes that the problem is linear, and the signal variance is higher than the noise. Therefore, we use PCA as a way to reduce our signal's noise with a clever choice of the components we keep. The result is a clean signal with most of its experimental and background noise removed, but this comes with a downside that has to be addressed: the ultimate decision of which components are relevant and which are not reside on the hands of the analyst who applies the method, a decision that is not always easy. On the one hand, leaving too many components still leaves undesired noise, while on the other hand, cutting too many components away means a loss of relevant physical information [6.4]. Figure 3 shows an example of the effect of PCA on a raw dataset.

G. b) Cluster analysis

Cluster analysis (or clustering for short) is a well-known procedure in data science and it aims to classify individual pixel spectra in groups according to similarity in attributes among them. The first step is turning our 3D data into a 2D dataset. This is accomplished through merging the position axes into the new position axis n as follows: $n = X \cdot Y$, which we will treat as our objects, versus our remaining dimension, the intensity value in each channel $p = E$, which is our attribute. In our new formed matrix $n \cdot p$ each individual spectrum is now a row, and it is now a suitable input for most data clustering algorithms.

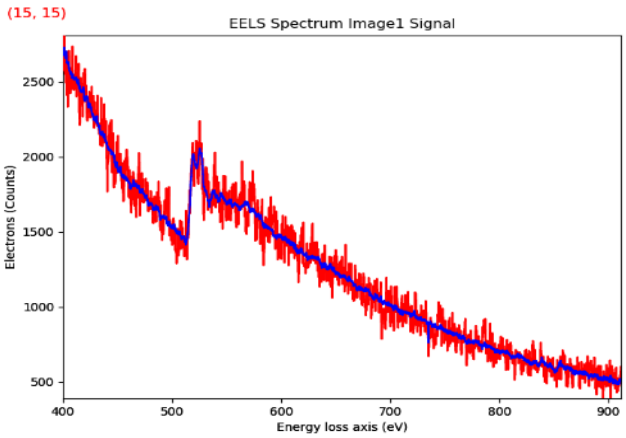

Figure 3. Comparison between a raw EEL spectrum (in red) and the same data once treated via Principal Component Analysis (in blue).

By considering the spectra in a spectrum image as a collection of p-dimensional points the algorithm can be easily applied to EELS data [34]. In addition, if we apply a noise reduction method such as the aforementioned PCA, and we only take a subset of components, computation time is greatly reduced. Finally, by assembling all spectra by similarities in shape, we can characterize the material setting the number of clusters, which will describe different zones of the sample. Studying the average spectrum of every cluster, we are now able to map composition vs position. One last thing to note is that clustering does not alter in any way the input data, making it a very powerful resource, because results are components with physical meaning.

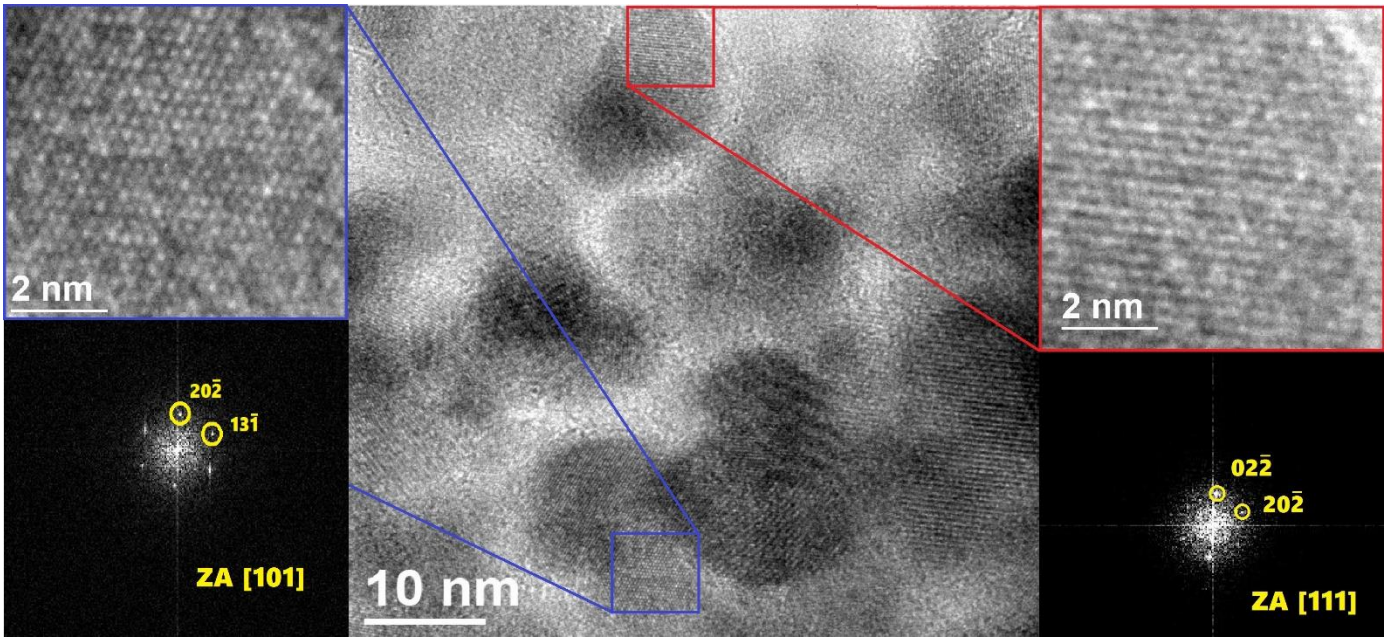

Figure 4. *(Left)* HRTEM image of a region of the sample, where a conglomerate of iron oxide nanoparticles can be observed. *(Right top)* Zoomed region of a single nanoparticle, where a more detailed crystallographic structure can be appreciated. *(Right bottom)* Fast Fourier transform (FFT) of the zoomed region, with its corresponding indexing and zone axis identification.

II. Experimental

This work aims to study the oxidation state of iron oxide nanoparticles. The sample was provided by the Nanobioengineering Laboratory of the Bioengineering Institute of Catalonia (IBEC). The preparation of the sample for the TEM consisted on dispersing those nanoparticles in ethanol through a sonicator. A drop was then deposited over a TEM copper grid to let dry at room temperature.

The spectrum images were obtained in the JEOL 2010-F electron microscope, which is located in the CCiT UB (Scientific and Technological Centres of the University of Barcelona). Several STEM-EELS spectrum images were acquired, in a process in which the electron beam was set at 200 kV, coupled to a Gatan imaging filter (GIF), the collection angle was 30 mrad, and the convergence angle was set to 15 mrad.

III. Results

A. Preliminary characterization

The first step in order to characterize the sample consists in the indexation of the crystallographic planes. In Figure 4 there can be seen the indexing of two distinct regions of the HRTEM image. The red region corresponds to an isolated nanoparticle, whereas the blue one conforms a region where multiple particles could be overlapped. Figure 5 shows the diffraction pattern of all the HRTEM image from Figure 4. A series of rings can be seen, corresponding to a set of families of planes. The fact that these families of planes configure rings and not fixed spots points to the fact that the nanoparticles have different orientations, and through the radius of each ring, the identity of each family can be identified. The indexing of the red region shows six spots, each of them situated at the same radius from the centre, showing the presence of only one family of planes, {220}. The blue region indexing, though, reveals also a hexagonal pattern, but with one pair of spots closer to the centre. As can be seen in Figure 4, contributions from orientations {220} and {311} are present.

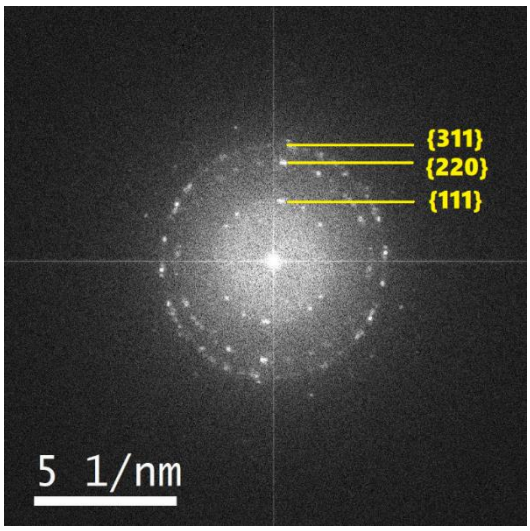

Figure 5. Fast Fourier transform of the entirety of the HRTEM image seen on Figure 4 (left), with the indexing of the families of planes that correspond to each ring of spots.

Knowing the interplanar distances for each family, seems direct to think that comparing those experimental measurements to the theoretical distances for different forms of iron oxide could prove useful to the determination of the composition of the sample.

Table 1. Experimental values for the interplanar space found through indexing, where ring 1 is the innermost ring and 3 the outermost, and theoretical tabulated values found for magnetite, maghemite and wurtzite unit cell, as well as the identification of the planes that generate those spots.

d_{hkl} (Å)	Fam. of planes	Exp.	Magnetite	Maghemite	Wurtzite
Ring 1	{111}	4.869	4.847	4.809	2.495
Ring 2	{220}	2.995	2.968	2.945	1.528
Ring 3	{311}	2.548	2.531	2.512	1.303

Table 1 shows the comparison between calculated values for magnetite and maghemite, but as it can be seen, it is hard to get a significative conclusion, the relative error is too much to identify one unique phase. In order to analyze the oxidation state of the sample, a much more detailed study will be needed, and EELS data treatment could shed some light to the problem.

B. EELS analysis

In order to manage the raw STEM-EELS data, a standard procedure has been performed, in which the dataset is despiked and background removed. Despiking consists in the removal of spikes, or sudden jumps in intensity for one energy channel, mainly due to the detector reading cosmic ray contributions. Those spikes cannot be avoided, so an algorithm that smooths

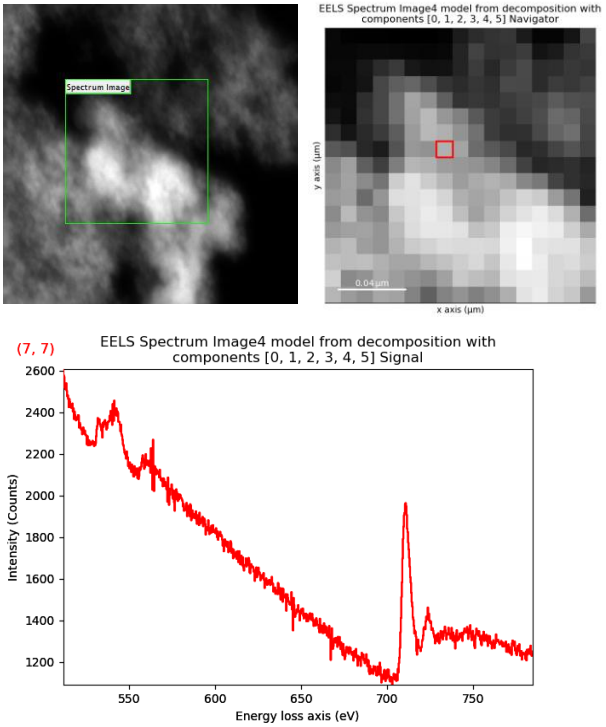

Figure 6. *(Up left)* Survey image of the region where EELS-STEM is applied. *(Up right)* Survey image with all pixels in which a spectrum has been collected. *(Bottom)* Spectrum associated to the pixel marked in red in the survey image in the upper right figure. The data is despiked and PCA has been applied to it for the first 6 components.

the sudden jump is a well-established way to proceed. The removal of the background consists in disposing of the contributions of the elements that are present in the core-loss region prior to the region we want to study. This is a way to set to zero all information that does not belong to the feature of the spectra one wants to analyse. Finally, Principal Component Analysis will help reducing the noise present in the data, after cleverly taking out some components while keeping others.

After these steps, the data is ready to be managed, but extracting the proper information is not always an easy task. Two ways of proceeding will be here discussed, being modelling through individual components and cluster analysis.

B. a) Clustering

Once the clustering algorithms have been run, significative results were obtained for 3 clusters. The reason is that less than this amount produced a lack of physical information, but over 3 clusters implied that there was always a redundant cluster adding no relevant data towards interpreting the results. So, Figure 6 reveals the result for the clustering algorithm for 3 clusters. It has to be noted that, in order for the clustering algorithm to be robust, removing the background is something that the analyst will want to do *after* applying the algorithm. That will help the algorithm sort spectra by similarity between pixels much easier, as the data will be less manipulated [34].

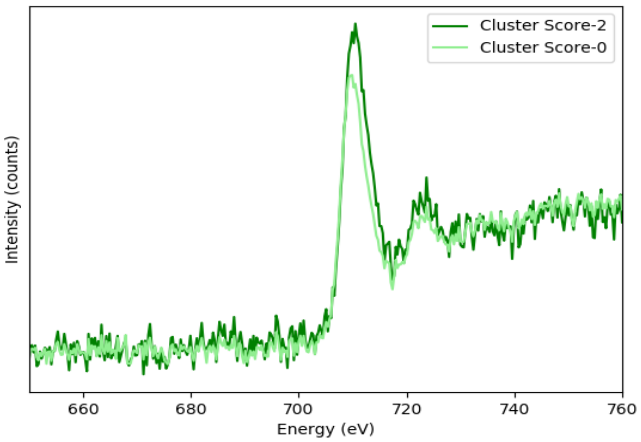

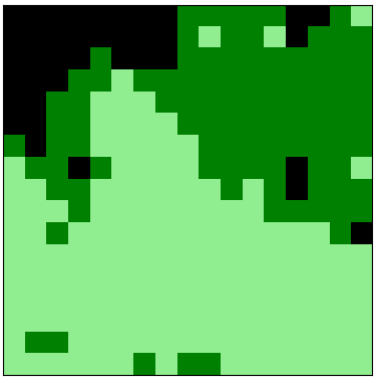

Figure 7. *(Up)* Graph with two spectra corresponding to the mean spectrum of each cluster painted with a shade of green (Background prior to the L_3 white line has been removed after the clustering process). *(Left)* Survey image reprinted in terms of the similarity from each pixel to the mean scores from the upper figure.

B. b) Model creation

As the main objective is to extract ELNES information from the $L_{3,2}$ white lines for the iron, another possible approach could be modelling the experimental data. By fitting a function to the experimental data, the desired information can be much easily extracted from the function that from the cloud of points. To get started, a clever set of components must be chosen. By choosing a series of simple, individual functions, the iterative algorithm can adjust the parameters of all of them until the result of the sum function fits the experimental data the closest. Obviously, the initial pick of components will play a crucial role, leading to a fast, successful fitting or failing to adjust otherwise. In order to fit the white lines, Lorentzian distributions have been chosen, as their more spread tail will help better fit the in-between of the white lines. Concerning the continuum contribution, an arctangent has been chosen, also modulated by a gaussian. This convolution of components far exceeds the quality of the fitting that Oxide Wizard was aiming for, as it used a linear contribution. The model creation consists in two parts: the first one adjusts a fitting function to just one pixel, which contains features that the analyst aims to study, and the second one, to all of them. This is so the first fitting serves as a starting point for the parameters of all contributions, which is useful not only in reducing the computing time, but also in avoiding in great measure the divergence of the fitting after the algorithm concludes. Figure 8 exemplifies a fitting over one pixel of our survey image with the aforementioned contributions.

The comparison of Fe $L_{3,2}$ ELNES for different iron oxidation states already allows qualitative statements about the valence [12, 21, 23-25]. It is well-known that oxidation states of iron can be determined by comparing the characteristics of both lines, for instance, the chemical shift or the comparison between the heights. As we performed a more or less rough fitting of the cloud of data, a comparison between the area under the curves for the Lorentzian distributions that fit both lines is the chosen comparison approach [21]. By integrating the curves using as limits in the

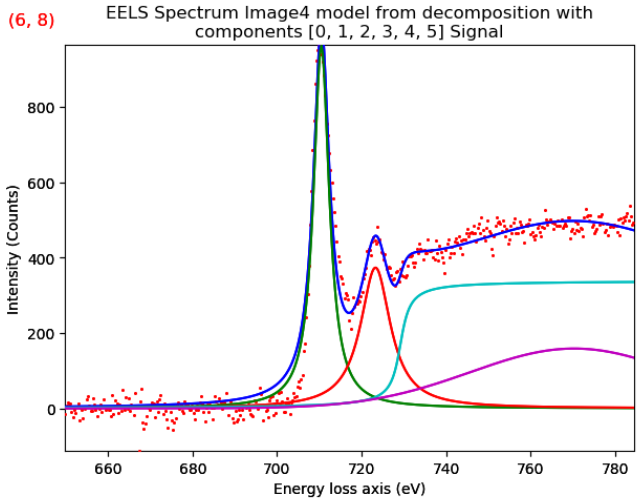

Figure 8. EELS raw data for the pixel (6,8) of the survey image from Figure6 (up right), as well as its corresponding function fit. Model for the fit comprised by: Lorentzian distributions for the white lines (in green for the L_3 and in red for the L_2), and an arctangent in cyan and a Gaussian distribution in magenta for the continuum.

energy axis the full-width half maximum, and dividing those areas, a map of the sample in terms of the area ratio can be extracted Figure 9 is the result of that mapping.

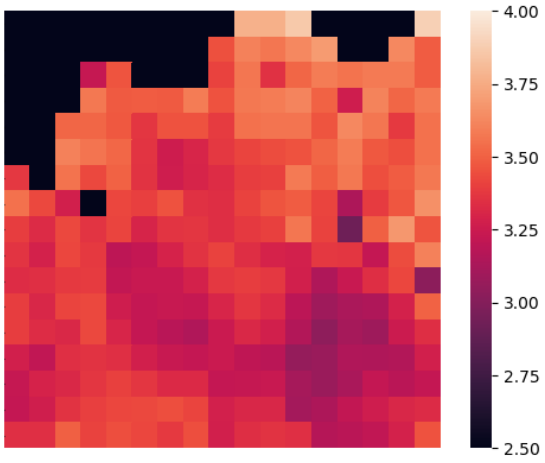

Figure 9. Color map of the survey image from Figure 6. The color scale measures the ratio L_3/L_2 of areas under the Lorentzian contributions to the fitting function of the model.

IV. Analysis and Discussion

Looking at Figure 10, it seems clear that there is a correlation between the results of both clustering and the ratio between areas under the Lorentzian distributions that fit the $L_{3,2}$ white lines. The two clusters in gray (ignoring the one in black, that corresponds to the background) seem to differentiate two distinct areas of the sample where the oxidation states vary. Figure 10 (right) shows how for the area which would correspond to the darkest shade of grey in Figure 10 (left), the ratio of areas for the L_3/L_2 lines stays approximately under the value 3.2, whereas for the region corresponding to the lightest gray cluster, it exceeds this value. Also, taking a look at the scores for the clustering in Figure 7 (up), a chemical shift is present between the scores, as well as a narrower and shorter L_3 for the lightest green spectrum. These results lead to the conclusion that the methodology used in this work has presented a map of oxidation states within our sample.

Thanks to the ratios in intensity found, we can compare with the literature in order to finally characterize the sample. In order

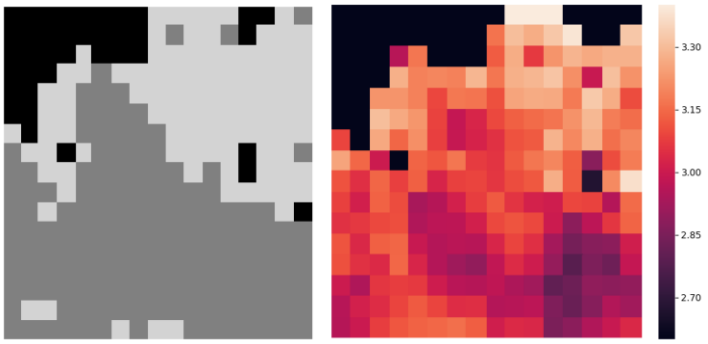

Figure 10. Side by side comparison of the results of the clustering algorithm from Figure 7, in a gray scale (left) and the area ratio treatment from Figure 9 (right).

to do so, we are going to refer to the work of Van Aken and Liebscher (2002) [25]. Figure 11 is an adaptation from their article, and it links a correlation between the $L_{3,2}$ intensity ratio in terms of the proportion of Fe^{3+} ions present in the sample. Based on our ratio, which roughly reaches 4, we obtain a composition that matches that of magnetite. The two distinct regions the clustering analysis point to, most likely seem to express how the outermost part of the sample has suffered some reduction. It must be noted that some discrepancies could arise between the results found and those in the literature, as the integration methods varies: for instance, the authors of our main article for comparing [25] opted for taking 2-eV windows instead of the fwhm, as well as fitting the white lines with a convolution of 4 Gaussian components. Future sights for this project would consist on the creation of our own reference chart, by applying this same procedure to an extended series of iron oxide structures.

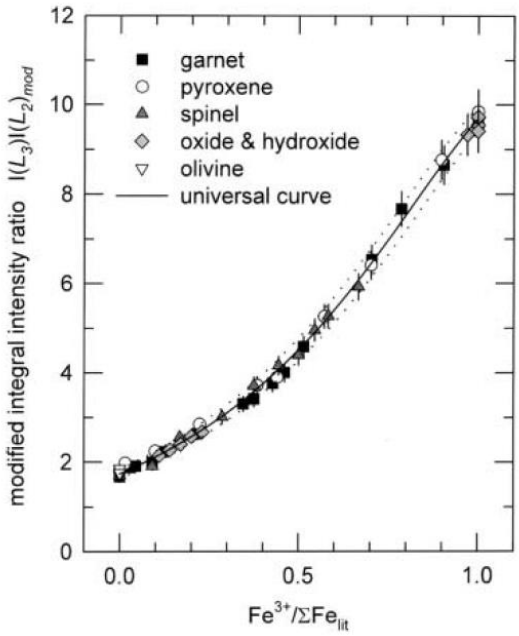

Figure 11. White-line intensity ratio versus ferric iron concentration using the 2-eV integration windows for garnets, pyroxenes, spinels, oxides, hydroxides and olivines. The solid line is the universal curve, described by a second-order hyperbolic function. The dotted lines represent the error range with $\Delta(Fe^{3+}/\Sigma Fe) = \pm 0.03$. Figure adapted from [23].

V. Conclusions

A sample of iron oxide nanoparticles has been characterized as magnetite nanoparticles by means of STEM-EELS data treatment. The combination of cluster analysis and modelling of a fitting function has been able to extract the needed information in order for us to successfully compare with the tabulated values in the literature.

In the end, an EELS data treatment has proven to be an efficient and reliable way to analyse valence states in iron oxides, and this can be extended to other transition metals. By the nature of this technique, as long as the EEL spectrum of the sample shows white line features, the algorithms could be

adapted, making this procedure one with a lot of potential in oxidation mapping. This versatility and its capability for managing huge datasets in a very reasonable amount of time makes this approach one of the best of its kind.

VI. ACKNOWLEDGEMENT

First of all, I would express my gratitude to Sònia Estradé and Francesca Peiró for directing this thesis, which has been as challenging to tackle as has been rewarding to finish.

I would also like to give a special thank you to my advisor Javier Blanco, who has helped me in every step of the road and who has been the person from which I have learned the most.

Finally, I would like to acknowledge all the researchers in the team LENS (and non-LENS people from the so-called "Despatx Patera") – Dani, Lluís, Juan Luis, Catalina, Julià…, who are more like a close family than a group of co-workers, and received me in their work space as one more of them.

VII. REFERENCES

[1] Ruthemann, G. - Naturwissenschaften 30, (1942).
[2] Pines, D., Bohm, D. - Phys. Rev. 82, 625, (1951).
[3] Fink J. - Transmission electron energy-loss spectroscopy. Fuggle J.C., Inglesfield J.E. (eds) - Unoccupied Electronic States. Topics in Applied Physics, vol 69. Springer, Berlin, Heidelberg, (1992).
[4] Egerton, R. F. - Electron Energy Loss Spectroscopy in the Electron Microscope. Springer. 3rd ed. New York, (2011).
[4.1] Chapter 1. [4.2] Chapter 1.2. [4.3] P. 124, eq (3.14). [4.4] P. 125, eq (3.15). [4.5] Chapter 3.1. [4.6] Chapter 3.8.
[5] Gatan corporate webpage - http://www.eels.info/about/techniques/eels-0 – Accessed on June 15th, 2019.
[6] Yedra, L. - Towards a new dimension in analytical TEM: EELS, Tomography and the Spectrum Volume. University of Barcelona, (2013).
[6.1] Chapters 5, 6. [6.2] P. 41. [6.3] Chapter 3.2. [6.4] Chapter 4.3.2.
[7] Lenz, F. - Zur Streuung Mittelschneller Elektronen in Kleinste Winkel (1954). Online publication: Zeitschrift für Naturforschung A, Vol. 9, Issue 3, pp 185-204 (2014).
[8] Inokuti, M. – Inelastic Collisions of Fast Charged Particles with Atoms and Molecules – The Bethe Theory Revisited. Rev. Mod. Phys. 43, 297 (1971).
[9] Cromer, D. T., Waber, J. T. – Scattering factors computed from relativistic Dirac-Slater wave functions. Acta Cryst, 18, pp. 104-109 (1965).
[10] Radtke, G., Botton, G. A. – Scanning Transmission Electron Microscopy, Imaging and Analysis (Chapter 5). Springer. Ed: Stephen J. Pennycock, Peter D. Nellist, pp. 207-217, (2005).
[11] Cottrell, E., Kelley, K. A., Lanzirotti, A., Fischer, R. A. – High precision determination of iron oxidation state in silicate glasses using XANES. Chemical Geology, vol. 268, issues 3-4, pp. 167-179 (2009).
[12] Rez, P., Bruley, J., Brohan, P., Payne, M., Garvie, L. A. J. – Review of methods for calculating near edge structure. Ultramicroscopy 59, pp. 159-167 (1995).
[13] Egerton, R. F., Malac, M. – EELS in the TEM. Journal of Electron Spectroscopy and Related Phenomena 143, pp. 43-50 (2005).
[14] Leapman, R. D., Grunes, L. A., Fejes, P. L. – Study of the $L_{2,3}$ edges in the 3d transition metals and their oxides by electron-energy-loss spectroscopy with comparisons to theory. Phys Rev. B 26, 614 (1982).
[15] Schmid, H. K., Mader, W. - Oxidation states of Mn and Fe in various compound oxide systems. Micron 37, pp. 426-432 (2006).
[16] Garvie, L. A. J., Craven, A. J. – High-resolution parallel electron energy-loss spectroscopy of Mn $L_{2,3}$-edges in inorganic manganese compounds. Physics and Chemistry of Minerals, vol. 21, issue 4, pp. 191-206 (1994).
[17] Daulton, T. L., Little, B. J. – Determination of chromium valence over the range Cr(0)-Cr(VI) by electron energy loss spectroscopy. Ultramicroscopy vol. 106, issue 7, pp. 561-573 (2006).
[18] Arévalo-López, A. M., Alario-Franco, M. A. - Reliable method for determining the oxidation state in chromium oxides. Inorg. Chem, 48, (2009).
[19] Loomer, D. B., Al, T. A., Weaver, L., Cogswell, S. – Manganese valence imaging in Mn minerals at the nanoscale using STEM-EELS. American Mineralogist 92, pp. 72-79 (2007).
[20] Paterson, J. H., Krivanek, O. L. – ELNES of 3d transition -metal oxides: II. Variations with oxidation state and crystal structure. Ultramicroscopy, vol. 32, issue 4, pp. 319-325 (1990).
[21] Cavé. L, Al, T., Loomer, D., Cogswell, S., Weaver, L. – STEM/EELS method for mapping iron valence ratios in oxide minerals. Micron 37, pp. 301-309 (2006).
[22] Tan, H., Verbeeck, J., Abakumov, A., Van Tendeloo, G. – Oxidation state and chemical shift investigation in transition metal oxides by EELS. Ultramicroscopy 116, pp. 24-33 (2012).
[23] Garvie, L. A. J., Buseck, P. R. – Ratios of ferrous to ferric iron from nanometric-sized areas in minerals. Nature 396, pp. 667-670 (1998).
[24] Van Aken, P. A., Liebscher. B., Styrsa, V. J. – Quantitative determination of iron oxidation states in minerals using Fe $L_{3,2}$-edge electron energy-loss near-edge structure spectroscopy. Phys. Chem. Minerals 25, pp. 323-327 (1998).
[25] Van Aken, P. A., Liebscher. B. – Quantification of ferrous/ferric ratios in minerals: new evaluation schemes of Fe $L_{3,2}$ electron energy-loss near-edge spectra. Phys. Chem. Minerals 29, pp. 188-200 (2002).
[26] Digital Micrograph 3.4 User Guide, from the Gatan corporate webpage (www.gatan.com). Accessed on June 24th, 2019.
[27] Yedra. Ll., Xuriguera. E., Estrader, M., López-Ortega, A., Baró, M. D., Nogués, J., Roldan, M., Varela, M., Estradé, S., Peiró, F. – Oxide Wizard: An EELS Application to Characterize the White Lines of Transition Metal Edges.
[28] Hyperspy webpage – www.hyperspy.org – Accessed on June 23rd, 2019.

[29] Pankhurst, Q., Hautot, D., Khan, N., Dobson, J. – Increased levels of magnetic iron compounds in Alzheimer's disease. Journal of Alzheimer's disease, vol. 13, issue 1, pp. 49-52 (2008)
[30] Muñoz, P., Humeres A. – Iron deficiency on neuronal function. BioMetals, vol. 25, issue 4, pp. 825–835 (2012).
[31] Smith, M. et al. - Increased Iron and Free Radical Generation in Preclinical Alzheimer Disease and Mild Cognitive Impairment. Journal of Alzheimer's Disease, vol. 19, issue 1, pp. 363–372, (2010).
[32] Everett, J. et al. - Ferrous iron formation following the co-aggregation of ferric iron and the Alzheimer's disease peptide β-amyloid. Journey of the Royal Society Interface, vol. 11, issue 95, p. 20140165, (2014).
[33] Yedra, L., Eljarrat, A., Arenal, R., Pellicer, E., Cabo, M., López-Ortega, a., …, Peiró, F. – EEL spectroscopic tomography: Towards a new dimension in nanomaterials analysis. Ultramicroscopy, vol. 122, pp. 12-18 (2012).
[34] Torruella, P., Estrader, M., López-Ortega, A., Baró, M. D., Varela, M., Peiró, F., Estradé, S. – Clustering analysis strategies for electron energy loss spectroscopy (EELS). Ultramicroscopy, vol. 185, pp. 42-48 (2018).